Ultrasound-Assisted Synthesis of Mesoporous ZnO Nanostructures of Different Porosities

Umapada Pal,[†] Chang Woo Kim, Nitin A Jadhav, and Young Soo Kang*

Department of Chemistry, Sogang University, No. 1 Shinsu-dong, Mapo-gu, Seoul 121-742, Korea

Received: May 11, 2009; Revised Manuscript Received: July 12, 2009

Mesoporous ZnO nanoparticles with average pore sizes of 2.5 and 14.3 nm were prepared by ultrasonic hydrolysis of zinc acetate at different ultrasound powers. Morphology, crystallinity, and porosity of the materials have been studied using transmission electron microscopy (TEM), X-ray diffraction (XRD), and BET nitrogen adsorption. Whereas a moderate ultrasound power favored the synthesis of well-crystalline mesoporous ZnO nanoparticles of triangular and hexagonal morphologies with very low density of lattice defects and small pore size, high ultrasound power generated mesoporous ZnO nanoparticles of arbitrary morphology with higher density of lattice defects. Photoluminescence behaviors and the mechanisms of formation of the two types of porous nanostructures are discussed.

Introduction

The unique characteristics of zinc oxide (ZnO) made it a key functional material with applications in gas sensing,[1−4] catalysis,[5−7] optoelectronics,[8,9] and biomedicine.[10,11] Nanostructured forms of ZnO receive even wider applications due to low dimension and high specific surface area. Varieties of ZnO nanostructures from nanoparticles, nanorods, and nanotriangles to nanoribbons have already been developed.[12−18] For catalytic applications high surface area of the nanostructures is an important prerequisite. On the other hand, to access the optimum surface area and adequate flow rates through the materials, a nanostructure with porous morphology is an additional important feature. Very recently porous nanostructures of metal oxides like ZnO,[19,20] SnO_2,[21] SiO_2,[22−24] and TiO_2[25−27] have been developed. Whereas for mesoporous SiO_2, mainly the soft templating techniques using block copolymers have been used, for mesoporous TiO_2, cationic surfactant[25] or block copolymer like F127 (Pluronic block copolymer $EO_{106}-PO_{70}-EO_{106}$) has been utilized.[28] On the other hand only a very few works have been published on the synthesis of mesoporous ZnO structures. Very recently Bhattacharyya and Gedanken have reported the synthesis of mesoporous ZnO and Ag−ZnO nanocomposites by microwave-assisted and sonochemical routes.[19,20] Gao and Wang[29] have reported the synthesis of cage and shell-like porous ZnO structures grown by self-assembly of ZnO nanocrystals.

In the present article, we report on the synthesis of mesoporous ZnO nanostructures of different shapes and porosities through sonochemical reactions without using any template or structure-directing agent. Both the shape and porosity of these porous structures depended on the dissipated power of the ultrasound. The nanostructures were characterized by X-ray diffraction (XRD), transmission electron microscopy (TEM), photoluminescence (PL), and nitrogen absorption isotherms. The mechanism of formation of the porous structures is discussed.

Experimental Section

All the solvents and precursors in the present work were used as received, without further purification. For the sonochemical reaction, 1.5 g of zinc(II) acetate dihydrate ($C_4H_6O_4Zn\cdot 2H_2O$; Aldrich, 98%) was mixed in 100 mL of *N*,*N*-dimethylformamide (DMF, Jin Chemicals) and deionized water (10%) mixture. After dissolving the precursor in the solvent, the solution was treated with an ultrasonic T-horn (Fisher Scientific) either at 150 or 300 W of dissipated power under Ar flow for 3 h. After ultrasonic treatment, the white colloidal solution was centrifuged and washed several times with ethanol (SK Chemicals). The sample prepared with moderate (150 W) ultrasound power was denominated as ZnO-M, and the sample prepared with high (300 W) ultrasound power was denominated as ZnO-H. Use of 10% water in DMF helps to get better yield and improve the stoichiometry of ZnO, as discussed by Vijaya Kumar et al.[30] Use of Ar flow during the sonochemical process was to generate higher temperature during the collapse of the cavitation bubbles, generating disorder structures due to incompleteness of the surface structure, leading to greater porosity of the products as has been explained by Bhattacharyya and Gedanken.[19]

The morphology and composition of the samples were studied using a Hitachi S-4300 scanning electron microscope attached with Jobin-Horiba 6853-H EMAX analytical system. Crystallinity and fine structure of the samples were studied using a Rigaku D'Max 2200 V X-ray diffractometer (Cu Kα radiation, $\lambda = 1.5406$ Å) and JEOL JEM 2100F field emission transmission electron microscope (FETEM). For the N_2 adsorption/desorption isotherms, an automated QUADRASORB "SI" analyzer of Quantachrome Instruments was utilized. The absorption and emission spectra of the samples were studied using an Agilent 8453 UV−vis spectrophotometer and the 325 nm excitation of a Hitachi F-7000 fluorescence spectrophotometer, respectively.

Results and Discussion

Figure 1 illustrates the XRD patterns of the as-prepared ZnO nanostructures. The peaks of the XRD patterns match well with the wutrzite phase of ZnO (JCPDF card no. 89-1397). Though both the as-prepared samples were highly crystalline, the crystallinity of the sample prepared with high ultrasonic power was inferior that of to the sample prepared with moderate ultrasonic power. The energy-dispersive X-ray analysis (EDAX) (Figure 2) of the samples revealed that they contain only zinc, oxygen, and trace of carbon. However, the stoichiometry of the

* Corresponding author. E-mail: yskang@sogang.ac.kr. Tel.: +82-2-705-8882. Fax: +82-2-701-0967.

[†] On leave from Universidad Autonoma de Puebla, Mexico.

10.1021/jp904377n CCC: $40.75
Published on Web 07/28/2009

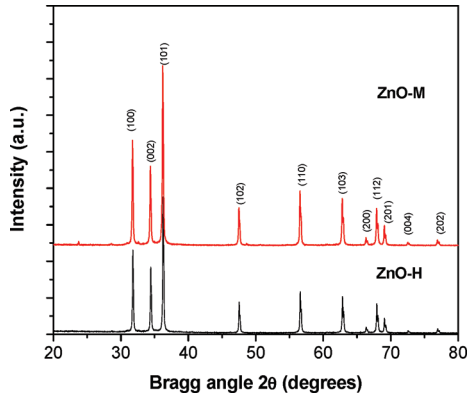

Figure 1. XRD spectra of the porous ZnO nanostructures.

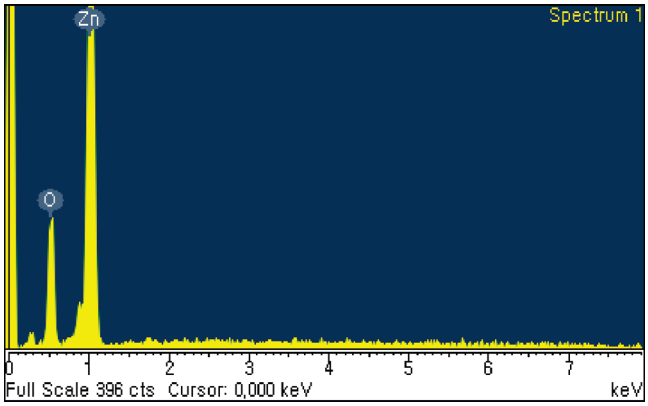

Figure 2. EDAX spectrum of the sample ZnO-H.

ZnO-M sample was better than that of the ZnO-H sample. The Zn/O atomic ratios for the ZnO-M and ZnO-H samples were 0.92 and 0.72, respectively. Figures 3 and 4 illustrate the typical TEM and high-resolution TEM (HRTEM) images of the samples prepared with moderate and high ultrasonic power, respectively. Whereas the formation of triangular and hexagonal nanostructures of about 120 nm dimension could be observed for the sample ZnO-M, nanoparticles of arbitrary shapes of about 200 nm size were formed in the sample ZnO-H. HRTEM images of the sample ZnO-M revealed small nanoparticles of about 3 nm size assembled (shown by arrows in Figure 3d) to form triangular or hexagonal morphologies with small interparticle spaces between them. On the other hand, the HRTEM images of the sample ZnO-H did not reveal the formation of such small particles (not presented). In contrast to the ZnO-M sample, the particles of the ZnO-H sample appear to be porous bulk structures. The pores that appeared in the ZnO-H sample are considerably bigger than in the sample ZnO-M. The crystalline nature of the small ZnO particles constructing the sample ZnO-M can be perceived clearly from the HRTEM image and fast Fourier transform (FFT) of selected area HRTEM shown in Figure 3g.

To asses the nature of pores and their average size in the samples, N_2 adsorption/desorption isotherms were recorded (Figure 5). Whereas the type II isotherm (IUPAC classification[31]) revealed for sample ZnO-M is due to monolayer−multilayer adsorption on the open surface of closed pores, the type IV isotherm with an H3 type hysteresis loop[31] is observed for the sample ZnO-H. The type IV isotherm for the latter sample is associated with the capillary condensation taking place in its mesopores. The H3 loop does not exhibit any limiting adsorption at high P/P_0 and is generally associated with aggregated particles. The average pore size estimated from the isotherms of ZnO-M and ZnO-H were about 2.5 and 14.3 nm, respectively. The estimated surface areas of ZnO-M and ZnO-H were of 2.95 and 5.54 m^3/g, respectively. To confirm the results the N_2 adsorption/desorption isotherms of the samples, the measurements were repeated two times on the samples prepared independently. However, the results were reproducible, confirming the effect of ultrasound power on the porosity of ZnO nanostructures.

To monitor the crystalline quality and defect structures in the porous nanostructures, their room-temperature PL and absorption spectra were recorded. The PL and absorption spectra of the as-grown samples are illustrated in Figure 6 and its inset, respectively. Whereas a sharp excitonic peak at about 376 nm appeared in the absorption spectrum of the ZnO-H sample, the peak was not so sharp for the sample ZnO-M. Moreover, an intense absorption tail is observed at the high-wavelength side for the sample ZnO-M revealing its high dispersive nature. As the nanostructures of sample ZnO-M were formed by self-assembly of small nanoparticles with certain disorders, such a dispersive absorption tail in their absorption spectrum is expected. On the other hand, as has been mentioned earlier, though the particles of the sample ZnO-H are larger in size, they appear to be bulklike, i.e., all the small particles in them are agglomerated or fused to form a porous single particle with bulklike characteristics. In that sense, the crystalline disorder in the sample ZnO-H is higher than that of the sample ZnO-M. This might be the reason for lower intensity of the XRD peaks in the ZnO-H sample than that of ZnO-M (Figure 1).

The crystalline disorder of the ZnO-H sample has also been reflected in its PL spectrum. As can be seen from Figure 6, the room-temperature PL spectrum of the ZnO-H sample consists of a near band edge peak at about 381 nm (3.25 eV) and a broad visible band with humps at about 415, 440, 470, and 542 nm. Whereas the near band edge emission peak was associated to the free excitonic transition in ZnO,[16] the 415 and 440 nm peaks are the components of the so-called blue emission in ZnO. The 470 and 542 nm peaks are associated to the so-called green and yellow emissions in ZnO, respectively. Whereas the green emission in ZnO has generally been associated to the oxygen vacancies (V_o) and interstitial zinc (Zn_i),[32−34] the blue emission in ZnO is associated to the native defects associated to V_o and V_{Zn}.[16,35] The yellow emission in ZnO (542 nm peak) has been associated to the oxygen excess.[36] The green emission at about 480 nm has also been frequently associated to the surface-deep traps in porous ZnO nanostructures.[37]

On the other hand, the PL spectrum of the sample ZnO-M, prepared with moderate ultrasound power, revealed a very strong near band edge emission with remarkably low visible emissions. Such PL features of the ZnO-M sample indicate its better crystallinity, lower density of lattice defects, and better stoichiometry. As the ZnO-H sample was synthesized with high ultrasound power, the formation of cavitation bubbles in the solution was vigorous and the temperature of the collapsing bubble was higher; which lead to the formation of highly disordered crystal structures than the sample prepared with moderate ultrasound power.

As is well-known, intense ultrasonic irradiation can produce cavitation leading to reactions like oxidation, reduction, dissolution, and hydrolysis.[38−40] The reactions can occur in three different regions[41] surrounding the collapse of a bubble like (a) the inner environment (gas phase) of the collapsing bubble, where high temperatures and high pressures are produced, causing the pyrolysis of water into H^+ and OH^- radicals, (b) the interfacial liquid region, i.e., at the interface of the cavitation

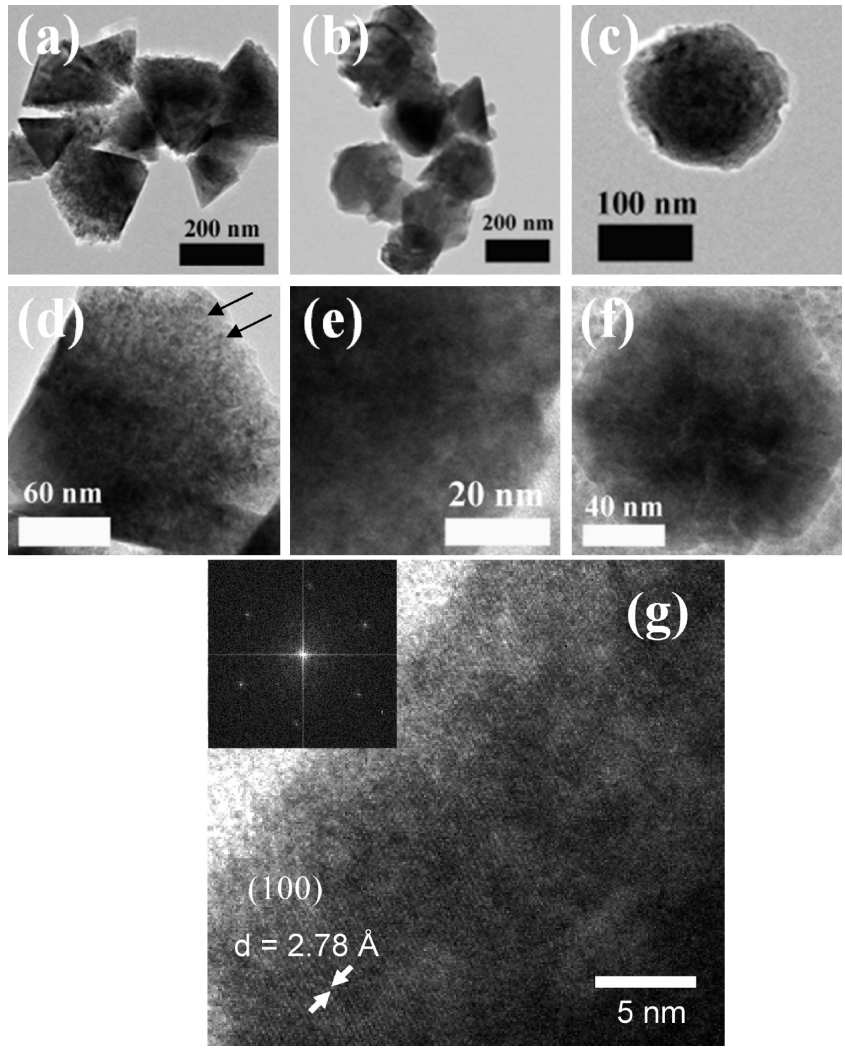

Figure 3. Typical TEM and HRTEM micrographs of the porous ZnO-M sample. Triangular and hexagonal morphologies of the porous nanostructures can be seen in panels a−f. Crystallinity of the nanoparticles forming the porous structure can be seen from the HRTEM and selected area FFT shown in panel g.

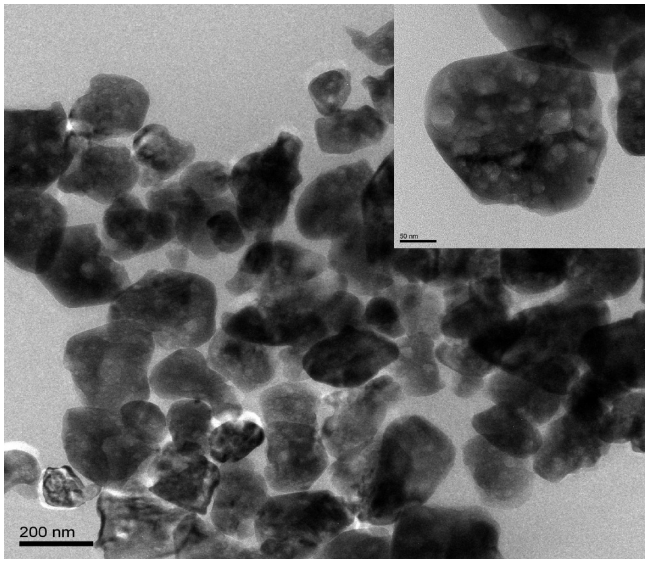

Figure 4. Typical TEM micrographs of the porous ZnO-H nanostructures.

bubble and the bulk solution with relatively lower temperature than the interior of the bubbles, and (c) in the bulk of the solution, which is at ambient temperature and pressure. Due to the ionic nature of zinc acetate and high tendency of hydroxyl radicals to concentrate in region b,[40] sonohydrolysis of zinc acetate is believed to occur in the interfacial region. Low viscosity, high surface tension, and low vapor pressure (3.7 Torr at 25 °C) of DMF favor the acoustic cavitation process, and the presence of 10% water in the solution enhances the hydrolysis rate of zinc acetate at the surface of the collapsing bubbles.

In the case of the sample prepared with moderate ultrasound power (ZnO-M), regular formation and collapsing of the cavitation bubbles occur, and the sonochemical hydrolysis of zinc acetate at the bubble surfaces occurs following the reaction:

$$Zn^{2+}(aq) + H_2O(l) \rightarrow ZnO(s) + 2H^+(aq)$$

Therefore, small ZnO nanoparticles of uniform size form following the shape and size of the collapsing bubbles (inter-bubble space). On the other hand, in the case of high ultrasound power (sample ZnO-H), production and collapsing of the cavitation bubbles are rapid processes, and the temperature at the surface of the collapsing bubbles is higher. Therefore, along with a rapid hydrolysis of zinc acetate, the formed ZnO nanoparticles get melted. Due to rapid collapsing and high vapor

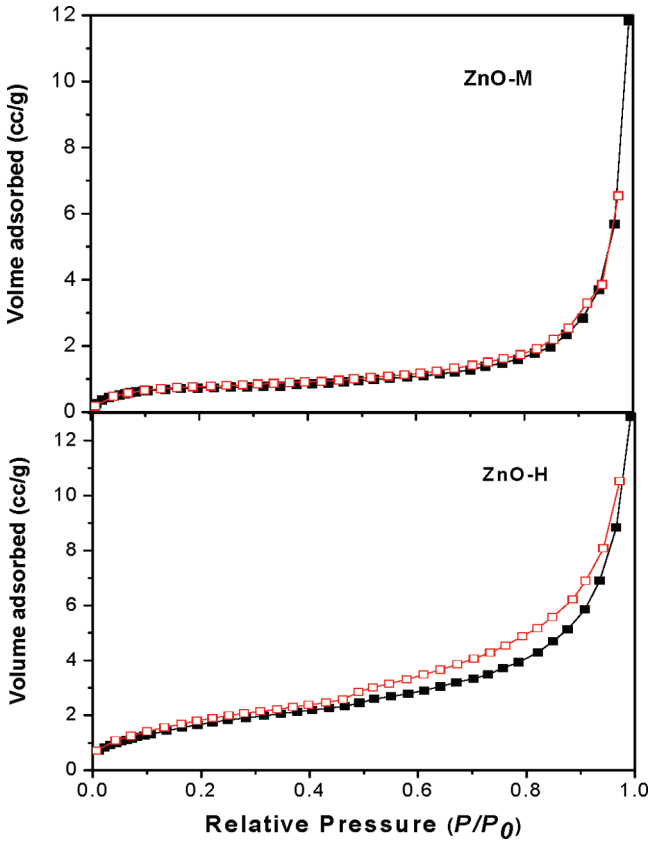

Figure 5. N_2 adsorption/desorption isotherms of the porous ZnO nanostructures: filled symbols, adsorption; open symbols, desorption. Estimated average BET pore size for ZnO-M and ZnO-H were 2.5 and 14.3 nm, respectively.

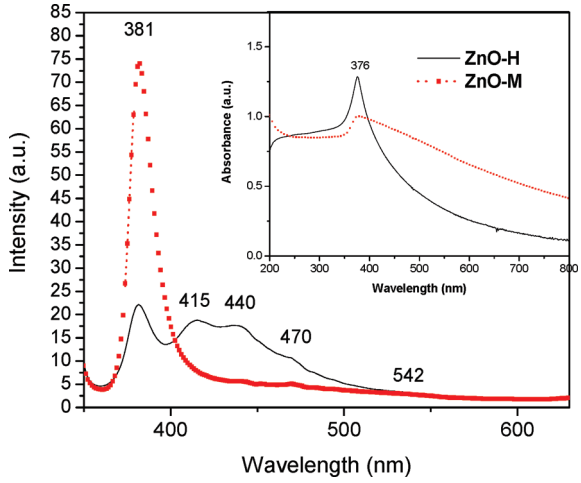

Figure 6. Room-temperature photoluminescence and absorption spectra of the porous ZnO nanostructures.

pressure at the interior of the bubbles, the shape and size of the collapsing bubbles alter; occasionally several bubbles collapse together. Such a high energy and highly irregular bubble collapsing process results in the formation of ZnO particles with bigger and irregular pores inside, as in the case of the sample ZnO-H. Moreover, due to the fusion of the initially formed ZnO particles at the surface of the collapsing bubbles, the resulting porous particles become singular entities with high lattice defects. It has been observed that application of ultrasound power below 100 W does not produce porous ZnO structures, and ultrasound power above 350 W drastically reduces the production yield.

Conclusions

Mesoporous ZnO nanostructures of different porosities can be fabricated by ultrasonic hydrolysis of zinc acetate. The pore size in the nanostructures can be controlled simply by varying the dissipated ultrasound power. Whereas a moderate ultrasound power generates mesoporous ZnO nanoparticles of triangular or hexagonal morphologies, high ultrasound power generates mesoporous ZnO nanoparticles of arbitrary shapes. Dissipated ultrasound power during the sonohydrolysis process controls the defect structures in ZnO nanostructures. Though a high ultrasound power generates ZnO nanoparticles of bigger average pore size, it incorporates several lattice defects leading to a degradation of their optoelectronic properties.

Acknowledgment. The work was financially supported through the Nano R&D Program (Korea Science & Engineering Foundation, Grant 2007-02628). U. Pal thanks Brain Pool Korea for financial support through the Brainpool program, and C. W. Kim acknowledges the financial support by the Brain Korea 21 project, 2009.

References and Notes

(1) Lim, H.-J.; Lee, D. Y.; Oh, Y.-J. *Sens. Actuators, A* **2006**, *125*, 404.
(2) Bie, L.-J.; Yan, X.-N.; Yin, J.; Duan, Y.-Q.; Yuan, Z.-H. *Sens. Actuators, B* **2007**, *126*, 604.
(3) Gao, T.; Wang, T. H. *Appl. Phys. A: Mater. Sci. Process.* **2005**, *80*, 1451.
(4) Fan, Z.; Lu, J. G. *Appl. Phys. Lett.* **2005**, *86*, 123510.
(5) Saito, M.; Fujitani, T.; Takeuchi, M.; Watanabe, T. *Appl. Phys. A: Mater. Sci. Process.* **1996**, *138*, 311.
(6) Evgenidou, E.; Fytianos, K.; Poulios, I. *Appl. Catal., B* **2005**, *59*, 81.
(7) Wang, Y.; Muhler, M.; Wöll, Ch. *Phys. Chem. Chem. Phys.* **2006**, *8*, 1521.
(8) Zhu, Y. W.; Zhang, H. Z.; Sun, X. C.; Feng, S. Q.; Xu, J.; Zhao, Q.; Xiang, B.; Wang, R. M.; Yu, D. P. *Appl. Phys. Lett.* **2003**, *83*, 144.
(9) Huang, M. H.; Mao, S.; Feick, H.; Yan, H.; Hu, Y.; Kind, H.; Weber, E.; Russo, R.; Yang, P. *Science* **2001**, *292*, 1897.
(10) Wang, Z. L. *J. Phys.: Condens. Matter* **2004**, *16*, R829.
(11) Wang, Z. L.; Song, J. *Science* **2006**, *312*, 242.
(12) Gao, P. X.; Ding, Y.; Mai, W.; Hughes, W. L.; Lao, C.; Wang, Z. L. *Science* **2005**, *309*, 1700.
(13) Qian, D.; Jiang, J. Z.; Hansen, P. L. *Chem. Commun.* **2003**, 1078.
(14) Ding, G. Q.; Shen, W. Z.; Zheng, M. J.; Fan, D. H. *Appl. Phys. Lett.* **2006**, *88*, 103106.
(15) Pal, U.; Santiago, P. *J. Phys. Chem. B* **2005**, *109*, 15317.
(16) Munoz Hernandez, G.; Escobedo Morales, A.; Pal, U. *Cryst. Growth Des.* **2009**, *9*, 297.
(17) Zhang, X. L.; Qiao, R.; Qiu, R.; Kim, J. C.; Kang, Y. S. *Cryst. Growth Des.* **2009**, *9*, 2906.
(18) Zhang, X. L.; Kang, Y. S. *Inorg. Chem.* **2006**, *45*, 4186.
(19) Bhattacharyya, S.; Gedanken, A. *Microporous Mesoporous Mater.* **2008**, *110*, 553.
(20) Bhattacharyya, S.; Gedanken, A. *J. Phys. Chem. C* **2008**, *112*, 659.
(21) Ba, J.; Polleux, J.; Antonietti, M.; Niederberger, M. *Adv. Mater.* **2005**, *17*, 2509.
(22) Kleitz, F.; Liu, D.; Anilkumar, G. M.; Park, I.-S.; Solovyov, L. A.; Shmakov, A. N.; Ryoo, R. *J. Phys. Chem. B* **2003**, *107*, 14296.
(23) Kang, Y.-S.; Lee, H. I.; Zhang, Y.; Jin, H. Y.; Yie, J. E.; Stucky, G. D.; Kim, J. M. *Chem. Commun.* **2004**, 1524–1525.
(24) Fan, J.; Yu, C.; Lei, J.; Zhang, Q.; Li, T.; Tu, B.; Zhou, W.; Zhao, D. *J. Am. Chem. Soc.* **2005**, *127*, 10794–10795.
(25) On, D. T. *Langmuir* **1999**, *15*, 8561.
(26) Crepaldi, E. L.; Soler-Illia, G. J. A. A.; Grosso, D.; Cagnol, F.; Ribot, F.; Sanchez, C. *J. Am. Chem. Soc.* **2003**, *123*, 9770.
(27) Grosso, D.; Soler-Illia, G. J. A. A.; Crepaldi, E. L.; Cagnol, F.; Sinturel, C.; Bourgeois, A.; Brunet-Bruneau, A.; Amenitsch, H.; Albouy, P. A.; Sanchez, C. *Chem. Mater.* **2003**, *15*, 4562.
(28) Sakatani, Y.; Grosso, D.; Nicole, L.; Boissie're, C.; Soler-Illia, G. J. A. A.; Sanchez, C. *J. Mater. Chem.* **2006**, *16*, 77.
(29) Gao, P. X.; Wang, Z. L. *J. Am. Chem. Soc.* **2003**, *125*, 11299.
(30) Vijaya Kumar, R.; Diamant, Y.; Gedanken, A. *Chem. Mater.* **2000**, *12*, 2301.

(31) Sing, K. S. W.; Everett, D. H.; Haul, R. A. W.; Moscou, L.; Pierotti, R. A.; Rouquerol, J.; Siemieniewska, T. *Pure Appl. Chem.* **1985**, *57*, 603.
(32) Studenikin, S. A.; Golego, N.; Cocivera, M. *J. Appl. Phys.* **1998**, *84*, 2287.
(33) Hu, Y.; Chen, H. J. *J. Appl. Phys.* **2007**, *101*, 124902.
(34) Sokol, A. A.; French, S. A.; Bromley, S. T.; Catlow, C. R. A.; van Dame, H. J. J.; Sherwoode, P. *Faraday Discuss.* **2007**, *134*, 267.
(35) Cheng, W.; Wu, P.; Zou, X.; Xiao, T. *J. Appl. Phys.* **2006**, *100*, 054311.
(36) Studenikin, S. A.; Golego, N.; Cocivera, M. *J. Appl. Phys.* **1998**, *84*, 2287.
(37) Gutierrez, M.; Henglein, A.; Dohrmann, J. *J. Phys. Chem.* **1987**, *91*, 6687.
(38) Song, R. Q.; Xu, A. W.; Deng, B'; Li, Q.; Chen, G. Y. *Adv. Funct. Mater.* **2007**, *17*, 296.
(39) Gutierrez, M.; Henglein, A. *J. Phys. Chem.* **1998**, *92*, 2978.
(40) Sostaric, J. Z.; Mulvaney, P.; Grieser, F. *Faraday Trans.* **1995**, *91*, 2847.
(41) Mason, T. J., Ed. *Advances in Sonochemistry*; JAI Press: London, 1993; Vol. 3.

JP904377N